The Astrophysical Journal Letters, 905:L7 (11pp), 2020 December 10 https://doi.org/10.3847/2041-8213/abca91

An 8.8 Minute Orbital Period Eclipsing Detached Double White Dwarf Binary

Kevin B. Burdge[1], Michael W. Coughlin[2], Jim Fuller[1], David L. Kaplan[3], S. R. Kulkarni[1], Thomas R. Marsh[4], Eric C. Bellm[5], Richard G. Dekany[6], Dmitry A. Duev[1], Matthew J. Graham[1], Ashish A. Mahabal[1,7], Frank J. Masci[8], Russ R. Laher[8], Reed Riddle[6], Maayane T. Soumagnac[9,10], and Thomas A. Prince[1]
[1] Division of Physics, Mathematics and Astronomy, California Institute of Technology, Pasadena, CA 91125, USA; kburdge@caltech.edu
[2] School of Physics and Astronomy, University of Minnesota, Minneapolis, MN 55455, USA
[3] Department of Physics, University of Wisconsin–Milwaukee, Milwaukee, WI 53211, USA
[4] Department of Physics, University of Warwick, Coventry CV4 7AL, UK
[5] DIRAC Institute, Department of Astronomy, University of Washington, 3910 15th Avenue NE, Seattle, WA 98195, USA
[6] Caltech Optical Observatories, California Institute of Technology, Pasadena, CA, USA
[7] Center for Data Driven Discovery, California Institute of Technology, Pasadena, CA 91125, USA
[8] IPAC, California Institute of Technology, 1200 East California Boulevard, Pasadena, CA 91125, USA
[9] Lawrence Berkeley National Laboratory, 1 Cyclotron Road, Berkeley, CA 94720, USA
[10] Department of Particle Physics and Astrophysics, Weizmann Institute of Science, Rehovot 76100, Israel
Received 2020 October 20; revised 2020 November 13; accepted 2020 November 13; published 2020 December 9

Abstract

We report the discovery of ZTF J2243+5242, an eclipsing double white dwarf binary with an orbital period of just 8.8 minutes, the second known eclipsing binary with an orbital period of less than 10 minutes. The system likely consists of two low-mass white dwarfs and will merge in approximately 400,000 yr to form either an isolated hot subdwarf or an R Coronae Borealis star. Like its 6.91 minute counterpart, ZTF J1539+5027, ZTF J2243+5242 will be among the strongest gravitational-wave sources detectable by the space-based gravitational-wave detector the Laser Space Interferometer Antenna (LISA) because its gravitational-wave frequency falls near the peak of LISA's sensitivity. Based on its estimated distance of $d = 2425^{+108}_{-114}$ pc, LISA should detect the source within its first few months of operation and achieve a signal-to-noise ratio of 63 ± 7 after 4 yr. We find component masses of $M_A = 0.323^{+0.065}_{-0.047}$ and $M_B = 0.335^{+0.052}_{-0.054}\ M_\odot$, radii of $R_A = 0.0298^{+0.0013}_{-0.0012}$ and $R_B = 0.0275^{+0.0012}_{-0.0013}\ R_\odot$, and effective temperatures of $T_A = 26,300^{+1700}_{-900}$ and $T_B = 19,200^{+1500}_{-900}$ K. We determine all of these properties and the distance to this system using only photometric measurements, demonstrating a feasible way to estimate parameters for the large population of optically faint ($r > 21\ m_{AB}$) gravitational-wave sources that the Vera Rubin Observatory and LISA should identify.

Unified Astronomy Thesaurus concepts: White dwarf stars (1799); Gravitational wave sources (677); Compact binary stars (283)

1. Introduction

The population of known double white dwarfs (DWDs) that will merge within a Hubble time (orbital periods $\lesssim$12 hr) has increased substantially over the last decade, in large part due to efforts such as the extremely low mass white dwarf (ELM) survey (Brown et al. 2010, 2012, 2013, 2016a, 2020; Kilic et al. 2011, 2012; Gianninas et al. 2015) and the Supernova Type Ia Progenitor (SPY) survey (Napiwotzki et al. 2003, 2020), several of which emit gravitational waves detectable with the Laser Space Interferometer Antenna (LISA; Amaro-Seoane et al. 2017). From 2018–2020, through massive expansions in densely sampled time-domain photometric measurements, the Zwicky Transient Facility (ZTF) has facilitated a rapid growth in the population of known DWDs with orbital periods under 1 hr (Burdge et al. 2020). Two of the sources discovered by ZTF so far, the eclipsing DWD binaries ZTF J1539+5027 ($P_b \approx 6.91$ minutes; Burdge et al. 2019a) and ZTF J0538+1953 ($P_b \approx 14.44$ minutes; Burdge et al. 2020), should be detected by LISA with a high signal-to-noise ratio (S/N), enabling precise parameter estimation using gravitational waves (Littenberg & Cornish 2019). Thus, using the gravitational-wave signal from such a system combined with electromagnetic constraints, we will be able to probe novel white dwarf (WD) physics, such as the efficiency of tides in these objects (Piro 2019).

Here we report the discovery of ZTF J2243+5242, a DWD binary with an orbital period of just 8.8 minutes, the second-shortest eclipsing binary system known at the time of discovery. It is a high-S/N LISA-detectable gravitational-wave source that should be detected within the first month of LISA's operation and reach an S/N of 63 ± 7 4 yr into the mission. Unique among the binary systems known at $P_b < 10$ minutes, this system likely consists of a pair of helium-core (He) or hybrid (helium/CO-core) WDs with a mass ratio near unity, suggesting that it will result in a merger (Marsh et al. 2004). This binary is also unique among known $P_b < 10$ minute systems because neither object is near to filling its Roche lobe (our inferred parameters suggest $\frac{R}{R_L} \approx \frac{2}{3}$ for both objects, where R is the volume-averaged WD radius, and R_L is the radius of the Roche lobe), indicating that the system is well detached. Here we discuss the properties of this system, its past and future evolutionary history, and prospects for the discovery of more such sources in the eras of LISA and the Vera Rubin Observatory (VRO; Ivezić et al. 2019).

2. Observations

Before we discuss the discovery and analysis of this object (Section 3), we briefly discuss the different data sets and observations that we used.

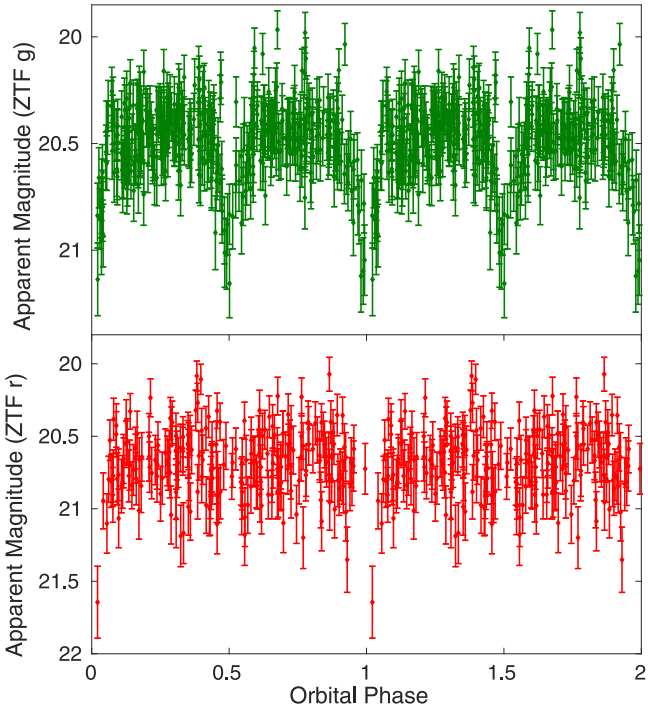

Figure 1. Archival ZTF g-band (top) and r-band (bottom) light curves of the system folded at a period of 527.934814 ± 0.000021 s. Because the system is 30% brighter in g-band than in r-band, and the ZTF is also slightly more sensitive in g-band, the discovery was enabled primarily by the g-band data.

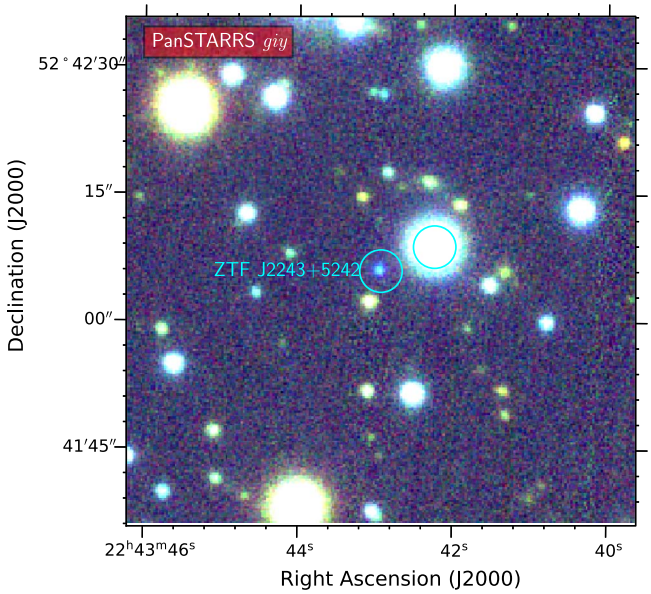

Figure 2. A 60″ × 60″ Pan-STARRS1 color giy-band image of ZTF J2243 +5242, which is the blue object in the center of the image. We illustrate 2.″5 apertures around the source and a nearby bright star in cyan. Due to the source's proximity to the bright star to the northwest (Gaia $G \approx 14.5$ m_V), we extracted forced difference image photometry for the ZTF light curve we used when modeling the source and PSF photometry for the CHIMERA high-speed photometry, and we used a 2.″5 aperture for extracting Swift UVOT photometry rather than the default 5″ radius.

2.1. ZTF Observations

The ZTF is a northern-sky synoptic survey based on observations with the 48 inch Samuel Oschin Schmidt telescope at Palomar Observatory (Bellm et al. 2019; Graham et al. 2019; Masci et al. 2019; Dekany et al. 2020). The camera has a 47 deg^2 field of view and reaches a 5σ limiting apparent magnitude of approximately 20.8 in the g band, 20.6 in the r band, and 20.2 in the i band, with standard 30 s exposures.

At the time of this writing, ZTF J2243+5242 had 218 r-band and 382 g-band good-quality photometric detections in its ZTF archival light curves. As illustrated by Figure 1, the discovery was enabled primarily by the g-band light curve, probably because the object is approximately 30% brighter in the g band than it is in the r band, and because ZTF is also more sensitive in the g band than in the r band (Masci et al. 2019). Note that the ZTF archive only contains 5σ detections in science images, but in order to model the ZTF light curve, after discovery, we extracted forced photometry from ZTF difference images to obtain the best-quality light curve possible (Yao et al. 2019). Using difference images helped improve the photometry significantly due to a nearby bright star to the northwest, as seen in the Pan-STARRS1 image cutout shown in Figure 2. The ZTF light curves extracted using forced photometry contained 1384 r-band and 827 g-band observations. The ZTF forced-photometry light curves contain substantially more epochs than the archival light curves, as the archival light curves only include 5σ detections of the source in science images. Additionally, the ZTF archival light curves are constructed by cross-matching 5σ detections in individual science exposures with a seed catalog generated by the ZTF reference image constructed from a coadd of ZTF images in each field. In the case of ZTF J2243+5242, this seed catalog generated from the reference image missed the source entirely in one field, meaning that all of the several hundred epochs of photometry in that field are completely absent in the ZTF archive, even the ones where the source was clearly detected at the 5σ level in individual exposures. It is possible that in ZTF Phase II, the data archive could be enhanced to include forced photometry and a more robust seed catalog based on Pan-STARRS1 or Gaia.

2.2. High-speed Photometry

We obtained high-speed photometric follow-up of the system using the dual-channel high-speed photometer CHIMERA (Harding et al. 2016) on the 200 inch Hale telescope at Palomar Observatory. We conducted a campaign of observations over several nights, using g' as the blue channel filter and alternating between r' and i' on the red channel. The phase-folded and binned light curves from these observations can be seen in Figure 3. We used a combination of 3 and 5 s exposure times due to variable conditions across our nights of observing. All CHIMERA data were reduced using a publicly available pipeline[11] with a newly implemented point-spread function (PSF) photometry mode to accommodate reductions for this object, which has a bright neighboring star. Because we were not read noise–limited, we operated the CCD in frame transfer mode using the conventional (as opposed to the electron multiplying) 1 MHz amplifier. On nights of poor seeing (>1″), we binned the readout 2 × 2 in order to reduce the read noise. For further details, please see Table 1.

2.3. Spectroscopic Follow-up

Using the Low Resolution Imaging Spectrometer (LRIS) on the 10 m W. M. Keck I telescope on Maunakea (Oke et al.

[11] https://github.com/mcoughlin/kp84

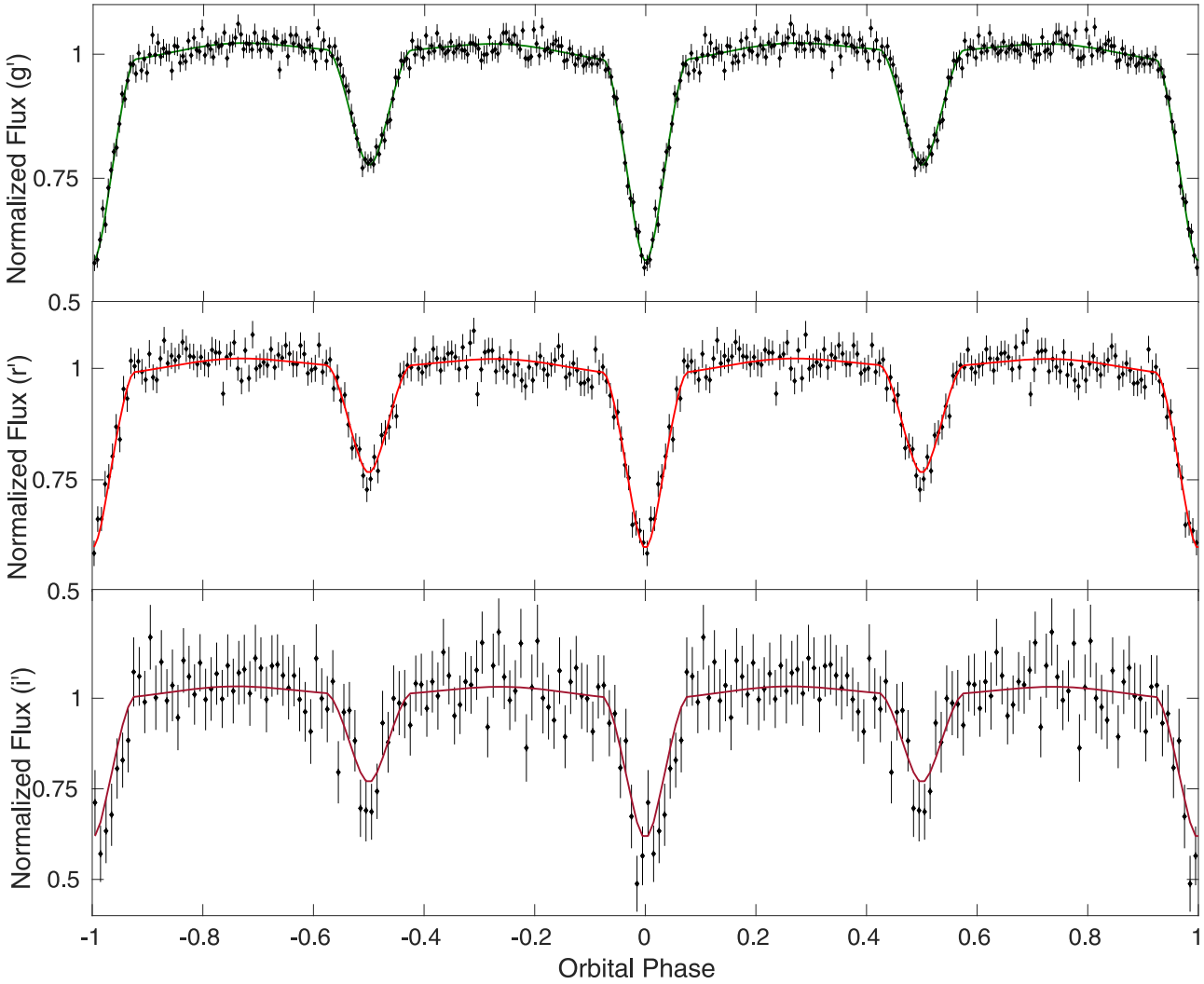

Figure 3. Binned, phase-folded CHIMERA g' (top), r' (middle), and i' (bottom) light curves of the system, with the best-fit LCURVE (Copperwheat et al. 2010) model overplotted.

1995), we conducted phase-resolved spectroscopy on the object. We used an exposure time of 66 s, about one-eighth of the orbital period, in order to avoid significant Doppler smearing over the course of an exposure. A coadded spectrum of one phase bin is illustrated in Figure 4. Due to issues with the red channel, we only analyzed data from the blue channel, which covered a wavelength range of approximately 3200–5500 Å. We used the 600/4000 grism as the dispersive element and binned the readout 4×4 in order to decrease the readout time to 30 s. We obtained a total of 312 exposures (see Table 1). We reduced the data with the publicly available lpipe pipeline (Perley 2019), and, in order to construct our phase-binned spectra, we divided the orbital phase into 12 bins and coadded all spectra with a mid-exposure time falling within each bin.

2.4. Swift Observations

We targeted the binary system with a 5075 s observation from the Neil Gehrels Swift Observatory on 2020 April 2 in order to obtain ultraviolet photometry for the source using the UVOT instrument (see Table 2), as well as an observation with the X-Ray Telescope (XRT; ObsID 00013301001; Gehrels et al. 2004). The UVOT observation used four exposures with lengths 448–1708 s, all with the UVM2 filter (centered at 2246 Å).

3. Discovery and Analysis

3.1. Photometric Selection

Like the systems described in Burdge et al. (2020), ZTF J2243+5242 was selected using a broad color cut using Pan-STARRS (Chambers et al. 2016), which encompassed all objects with $g - r < 0.2$ and $r - i < 0.2$ (see Burdge et al. 2020 for further details). As seen by the apparent magnitudes listed in Table 2, the object's temperature is large enough that it has a color of $g - r \approx -0.21$ and thus could have been targeted with a more restrictive selection. Currently, it is feasible to systematically search a broad selection, but in the VRO era, more restrictive selections may prove valuable in reducing the number of candidates. It is worth noting that the only two binary systems with even shorter orbital periods, HM Cnc (Ramsay et al. 2002) and ZTF J1539+5027 (Burdge et al. 2019a), also exhibit exceptionally blue Pan-STARRS1 colors of $g - r \approx -0.28$ and -0.39, respectively. Unlike HM Cnc and ZTF J1539+5027, which are both substantially brighter in the ultraviolet than in the optical, ZTF J2243+5242 is fainter in

Table 1
Table of Observations

Telescope	Instrument	Filter/Mode	Date (UTC)	No. of Exposures	Exposure Time (s)
Palomar 48 inch	ZTF	ZTF g	2018 Apr 24–2020 Sep 5	827	30
Palomar 48 inch	ZTF	ZTF r	2018 Apr 9–2020 Sep 4	1384	30
Palomar 200 inch	CHIMERA	g'	2020 Jul 15	1500	5
Palomar 200 inch	CHIMERA	g'	2020 Jul 21	4100	5
Palomar 200 inch	CHIMERA	r'	2020 Jul 21	4100	5
Palomar 200 inch	CHIMERA	g'	2020 Jul 23	5000	3
Palomar 200 inch	CHIMERA	i'	2020 Jul 23	2100	5
Palomar 200 inch	CHIMERA	g'	2020 Aug 19	6800	3
Palomar 200 inch	CHIMERA	r'	2020 Aug 19	4100	5
Palomar 200 inch	CHIMERA	g'	2020 Oct 16	2000	3
Keck I	LRIS	Blue arm	2020 Jul 18	165	66
Keck I	LRIS	Blue arm	2020 Sep 16	147	66
Swift	UVOT	UVM2	2020 Apr 2	4	5075
Swift	XRT	PC	2020 Apr 2	1	5075

these bands due to modest extinction resulting from its location in the Galactic plane ($b \approx -5.^{\circ}5$).

3.2. Period Finding

Object ZTF J2243+5242 was discovered using a graphics processing unit (GPU)–based implementation of the conditional entropy algorithm (Graham et al. 2013) in the cuvarbase package,[12] executed on four Nvidia 2080 Ti GPUs. Notably, because the system exhibits two similar depth eclipses, it was detected at half its period (≈4.4 minutes), and until we obtained follow-up photometry, it was unclear whether the object had a 4.4 or 8.8 minute orbital period.

3.3. Swift UVOT and XRT Results

In the Swift UVOT data, we could see ZTF J2243+5242 in the images, but there was a brighter source about 7.″5 to the northwest that complicated the photometry. Rather than use the default aperture of 5″ radius (where the PSFs overlap), we measured the photometry for ZTF J2243+5242 using a 2.″5 radius. We first summed the individual exposures using `uvotimsum` and then performed aperture photometry with a 2.″5 radius using `uvotsource`, with a nearby region with radius 40″ used to define the background. We find a source magnitude of $20.73 \pm 0.10\, m_{AB}$ for ZTF J2243+5242, which has been corrected to 5″ radius using the default PSF present in the Swift `CALDB`. We include a systematic uncertainty of 0.05 mag to account for standard Swift processing, as well as our nonstandard aperture choice.

For the Swift XRT data, there was no obvious emission present at the position of ZTF J2243+5242. There is one event within a circle with radius 9″ (the half-power point of the XRT) centered on ZTF J2243+5242. This was entirely consistent with background emission, where we find a mean of 0.58 counts in similar circles randomly distributed across the image. Therefore, we can set a 3σ upper limit of 3 counts in 5044 s, or a rate limit of $<0.6 \times 10^{-3}$ counts s^{-1}.

[12] https://github.com/johnh2o2/cuvarbase

3.4. Light Curve+SED Modeling and Parameter Estimation

We modeled ZTF J2243+5242 by fitting the CHIMERA light curve with a model generated using LCURVE (Copperwheat et al. 2010) while simultaneously fitting the Pan-STARRS1 and Swift photometry listed in Table 2. Here we describe this modeling procedure in detail.

Our overall modeling procedure sampled over 14 free parameters: the component masses M_A and M_B, temperatures T_A and T_B, volume-averaged radii R_A and R_B, orbital inclination i, time of superior conjunction T_0, period P_b, period derivative $\dot{P}_b$, distance to the system d, and three absorption parameters, α_g, α_r, and α_i, which describe the reprocessing of radiation that occurs when the stars irradiate each other. We fixed the gravity and limb-darkening coefficients using the work described in Claret et al. (2020a) using a four-parameter limb-darkening law (Claret 2000). We estimate the Doppler beaming coefficients for the system based on Claret et al. (2020b). In order to reduce the model dependence of the analysis, we did not invoke WD mass–radius relations, as was done in Burdge et al. (2020), but instead rejected any samples in which the smaller mass component in the system was also the hotter and smaller in radius, as these solutions would be physically inconsistent with a WD equation of state.

After constructing a likelihood function based on these free parameters, we performed our sampling using the nested sampling package Multinest (Feroz et al. 2009). We used an evidence tolerance of 0.5 with 1000 live points. A final model fit to the CHIMERA g', r', and i' data using the parameters reported in Table 3 is illustrated in Figure 3. Corner plots from this comprehensive analysis, showing the covariance between parameters, are illustrated in Figure 5. Note that for ease of reading, we have omitted some free parameters, such as T_0, P_b, $\dot{P}_b$, and the absorption coefficients. The final parameters we derived from the analysis are reported in Table 3. The remainder of this section discusses how we constructed our likelihood function and other details of our sampling procedure.

Light-curve fit. We simultaneously fit the CHIMERA g', r', and i' and ZTF r- and g-band light curves from all nights,

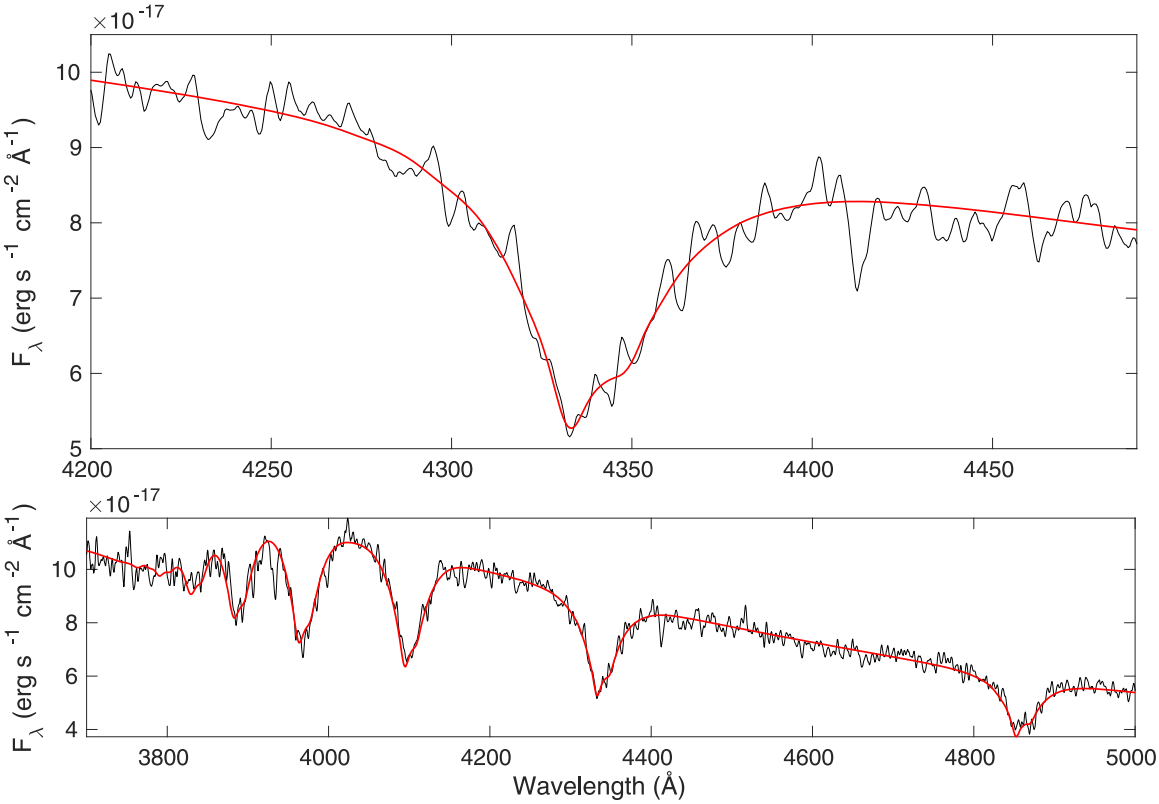

Figure 4. Example of a spectroscopic model fit to a phase-binned spectrum of ZTF J2243+5242. Such fits were performed on 12 phase-binned spectra and used a composite spectrum of two WD models with relative luminosity contributions and effective surface temperatures fixed by light-curve modeling. The splitting seen in the line cores is indicative that the system is double-lined. We did not measure radial velocities from these spectra due to the low S/N.

Table 2
Photometric Apparent Magnitudes and Astrometry

Survey	Filter/Quantity	Measured Value
Swift UVOT	UVM2	$20.73 \pm 0.15\ m_{AB}$
Pan-STARRS1	g	$20.359 \pm 0.029\ m_{AB}$
Pan-STARRS1	r	$20.571 \pm 0.027\ m_{AB}$
Pan-STARRS1	i	$20.733 \pm 0.024\ m_{AB}$
Pan-STARRS1	z	$20.92 \pm 0.12\ m_{AB}$
Gaia	G	$20.635 \pm 0.016\ m_{\rm V}$
Gaia	R.A.	$340.^{\circ}929043146 \pm 1.05$ mas
Gaia	Decl.	$+52.^{\circ}701660186 \pm 0.85$ mas
Gaia	Parallax	-1.57 ± 1.05 mas
Gaia	pm R.A.	$+0.48 \pm 2.29$ mas yr^{-1}
Gaia	pm Decl.	-5.12 ± 2.10 mas yr^{-1}
	$E(g-r)$	$0.16 \pm 0.02\ m_{AB}$

Note. Reddening estimated using distance reported in Table 3, with extinction maps of Green et al. (2019).

Table 3
Physical Parameters

Quantity	Measured Value
M_A	$0.323^{+0.065}_{-0.047}\ M_{\odot}$ (LC) $0.317^{+0.074}_{-0.074}\ M_{\odot}$ (Spect)
M_B	$0.335^{+0.052}_{-0.054}\ M_{\odot}$ (LC) $0.274^{+0.047}_{-0.047}\ M_{\odot}$ (Spect)
R_A	$0.0298^{+0.0013}_{-0.0012}\ R_{\odot}$
R_B	$0.0275^{+0.0012}_{-0.0013}\ R_{\odot}$
T_A	$26,300^{+1700}_{-900}$ K (SED) $26,520^{+130}_{-130}$ K (Spect)
T_B	$19,200^{+1500}_{-900}$ K (SED) $19,670^{+100}_{-100}$ K (Spect)
i	$82.^{\circ}12^{+0.51}_{-0.38}$ deg
a	$0.1227^{+0.0025}_{-0.0024}\ R_{\odot}$
K_A	455^{+66}_{-66} km s^{-1}
K_B	521^{+84}_{-84} km s^{-1}
γ	6^{+62}_{-62} km s^{-1}
T_0	$59,053.3448647^{+0.0000021}_{-0.0000022}$ MBJD$_{TDB}$
P_b	$527.934890^{+0.000032}_{-0.000033}$ s
$\dot{P}_b$	$1.37^{+0.12}_{-0.14} \times 10^{-11}$ s s^{-1}
d	2425^{+108}_{-114} pc

Note. Measured component and orbital parameters for ZTF J2243+5242. All parameters are derived from a combined analysis of the SED and CHIMERA light curves, with the exception of T_A and T_B, for which we also report estimates based on the optical spectrum of the system. The component parameters given here are the masses M_A and M_B, radii R_A and R_B, and surface temperatures T_A and T_B. We also report the distance to the system d and orbital parameters including the semimajor axis a, inclination i, radial velocity semiamplitudes K_A and K_B, systemic velocity γ, time of superior conjunction T_0, and orbital period P_b and its derivative $\dot{P}_b$. For the temperature estimates, T_A and T_B, we give estimates both based on a spectroscopic fit (Spect) and based purely on the spectral energy distribution (SED).

allowing each passband a free parameter representing the absorption coefficient (to model the reprocessing of radiation that arises from the stars irradiating the other, which is generally wavelength-dependent). All other free parameters were the same for the light-curve models of the three bands. Although the ZTF data have much lower S/Ns than the CHIMERA data, they were fit alongside the CHIMERA data because they strongly constrain the orbital period and its derivative due to their temporal baseline.

SED fit. We also use the parameters we sample over to generate a synthetic SED by computing a synthetic WD model atmosphere using Tremblay et al. (2011) with Stark broadening

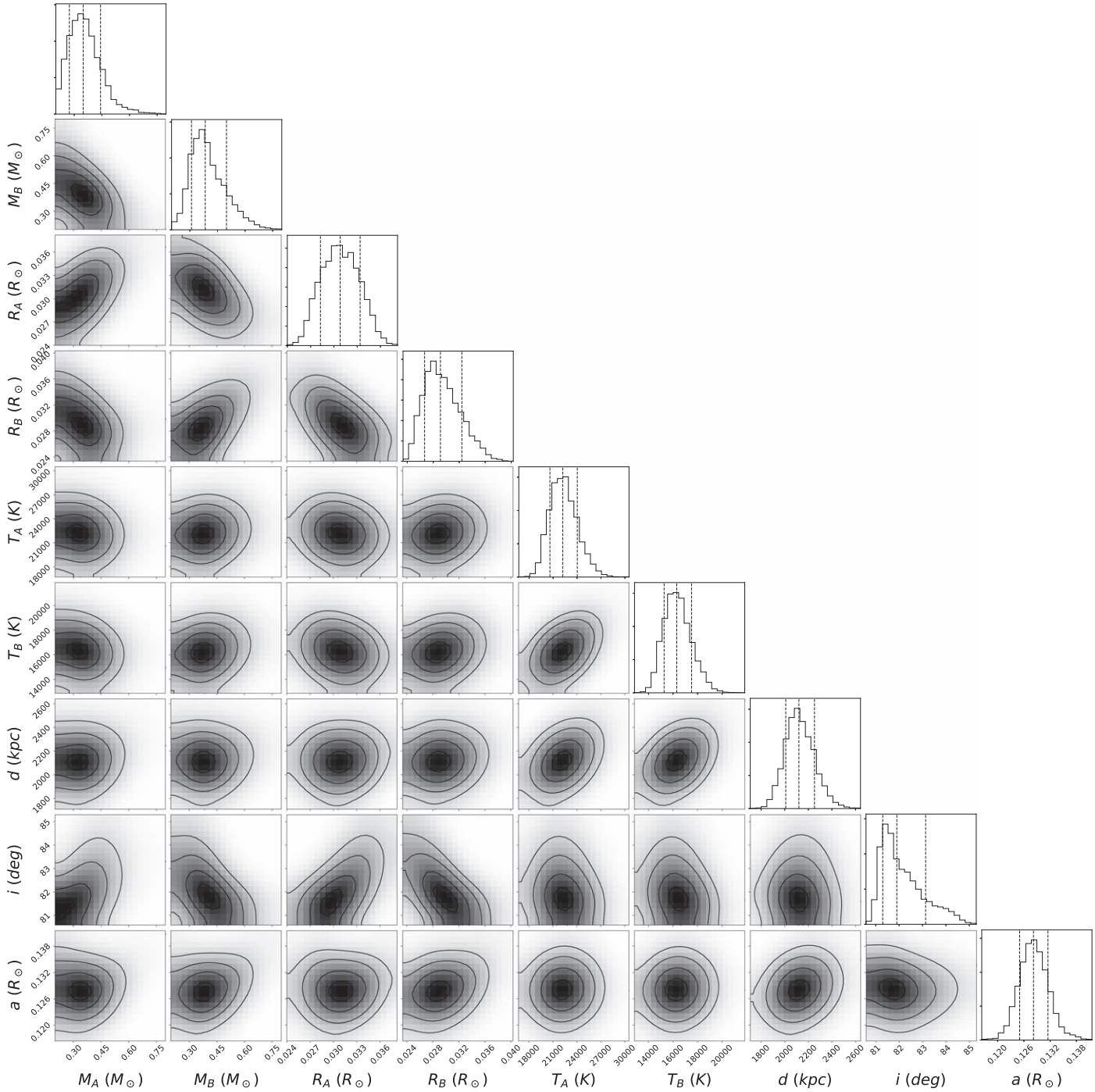

Figure 5. Corner plots illustrating the covariances of quantities estimated during our combined analysis. Note that for readability, we have omitted some parameters, including the time of superior conjunction T_0, the orbital period P_b, it is derivative $\dot{P}_b$, and the absorption coefficients.

from Tremblay & Bergeron (2009), and we use these synthetic spectra to compute the photometry for our passbands. Because we sample over the masses and radii of the components, for each iteration, we can compute the surface gravity of both objects, and by using these in combination with the temperatures of both objects (which we also sample over) and the radii and distances to the objects, we have all the degrees of freedom needed to compute synthetic photometry for these objects. We compute the reddening for each iteration by querying the extinction maps of Green et al. (2019), supplying the distance of each sample to estimate the reddening for that particular iteration (which we then use to redden our synthetic photometry in order to correctly fit the SED).

Ephemeris constraint. We fit for the time of superior conjunction, T_0, which is well constrained by the deep primary eclipse in the CHIMERA data (whose sharp ingress and egress allow for a precise measurement of the mid-eclipse time). We also fit for the orbital period P_b and its derivative, $\dot{P}_b$. The latter two parameters are primarily constrained by ZTF forced photometry (Yao et al. 2019), with its 2 yr baseline. We should be able to measure these parameters more precisely with continued monitoring of the system using high-speed

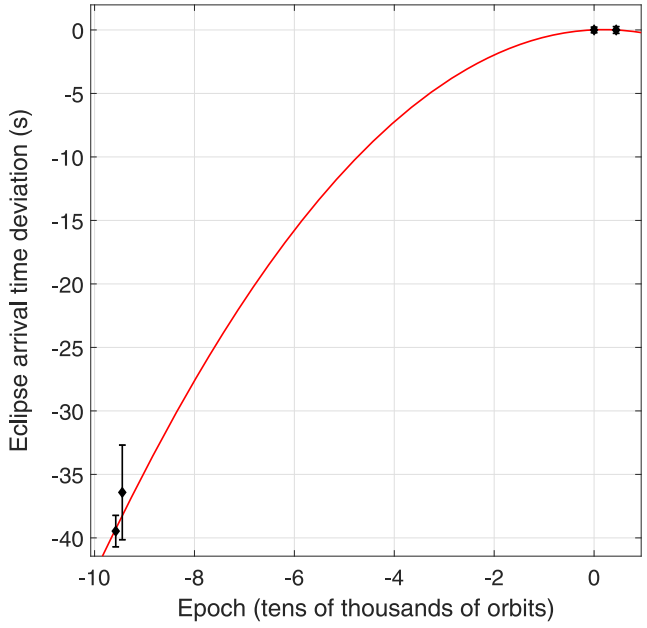

Figure 6. Eclipse timing of ZTF J2243+5242, demonstrating its orbital decay. The two black diamonds on the right (with small error bars) illustrate eclipse times derived from CHIMERA data, whereas the two points at much earlier times are derived from 2 nights of ZTF data, each of which contains over 3 hr of continuous observations of the source. The overplotted red parabola illustrates the predicted orbital evolution based on our derived $\dot{P}_b$.

photometers like CHIMERA, but at present, the baseline of the CHIMERA observations is short enough that the ZTF provides a far better constraint. We would like to note that unlike Burdge et al. (2019a, 2019b), we measured the $\dot{P}_b$ for this system by fitting for the parameter in our light-curve model, rather than constructing a diagram like the one shown in Figure 6 and fitting a quadratic to it. The reason for this is that there is a significant amount of ZTF data distributed throughout the last 2 yr that contains information about the orbit between the period when the CHIMERA data was obtained and the two densely sampled ZTF nights; thus, we decided to model all of the data coherently.

Mass constraints. In sampling over masses for the two WDs, we used a uniform prior of 0.15–0.7 $M_\odot$ in order to speed up sampling. Our final mass estimates converged within these boundaries, indicating that we did not need to widen this prior to consider lower- or higher-mass solutions. The masses are primarily constrained by ellipsoidal modulation in the light curve and the orbital decay of the system.

Because we fit the ZTF light curves (with their long baseline) in combination with our CHIMERA data, we are able to place tight constraints on the orbital period P_b and orbital period derivative $\dot{P}_b$. This allows us to constrain masses by assuming that the orbit is evolving according to energy loss due to gravitational-wave emission,

$$\dot{f}_{\rm GW} = \frac{96}{5}\pi^{\frac{8}{3}}\left(\frac{G\mathcal{M}}{c^3}\right)^{\frac{5}{3}} f_{\rm GW}^{\frac{11}{3}} \tag{1}$$

(Taylor & Weisberg 1989), where the chirp mass is given by $\mathcal{M} = \frac{(M_A M_B)^{\frac{3}{5}}}{(M_A + M_B)^{\frac{1}{5}}}$, and the gravitational-wave frequency is twice the orbital frequency, $f_{\rm GW} = \frac{2}{P_b}$.

We use the assumption that the orbital decay is due to general relativity to place an upper bound on $\mathcal{M}$; however, it is predicted that tidal effects could significantly contribute to the evolution of a binary at these short orbital periods, and thus we estimate an additional fractional tidal contribution of approximately 7.5% based on Equation (9) of Burdge et al. (2019a), where we have taken $\kappa_A = 0.12$ and $\kappa_B = 0.12$, which are constants determined by the internal structure of each WD. We estimated these values based on simulations performed in Burdge et al. (2019a), which estimated $\kappa \approx 0.11$ for the lower-mass He WD in ZTF J1539+5027 and $\kappa \approx 0.14$ for the CO WD in the system (in our case, the two WDs fall between these two and likely have a structure more similar to the He WD in ZTF J1539+5027). In any case, this approximation leads to an estimated tidal contribution of up to 7.5%, and we use this constraint to place a lower bound on the chirp mass. Thus, when we sample, we sample over $\dot{P}_b$, which is fit by the light curves, and we also estimate a purely relativistic $\dot{P}_{b_{\rm GW}}$ based on our masses M_A and M_B for that sample and reject any solutions falling outside the range $\dot{P}_b < \dot{P}_{b_{\rm GW}} < 0.925 \times \dot{P}_b$ to allow for solutions to the masses that accommodate up to a 7.5% tidal contribution to the orbital evolution.

In addition to the chirp mass constraint discussed above, these masses are also constrained by the fractional amplitude of ellipsoidal variations in the light curve, which are given by

$$\frac{\Delta F_{\rm ellipsoidal}}{F} = 0.15\frac{(15+u)(1+\tau)}{3-u}\left(\frac{R}{a}\right)^3 q\sin^2(i) \tag{2}$$

(Morris 1985), where u is the linear limb-darkening coefficient, τ is the gravity-darkening coefficient in the system, and $q = \frac{M_B}{M_A}$ is the mass ratio of the system. In ZTF J2243+5242, the ellipsoidal variations exhibit a semiamplitude of approximately 1.5%, which is quite small compared to systems like ZTF J1539+5027. This helps constrain the masses by driving the mass ratio q toward unity.

Inclination and radius constraints. In addition to constraining the mass ratio q and the T_0, modeling the CHIMERA light curve allows us to precisely estimate the inclination, i, and the ratio of the component radii, R_A and R_B, with respect to the semimajor axis, a. These constraints arise primarily from the total duration of the eclipses and the duration of ingress/egress. Because we also sample over masses, we are able to directly constrain the semimajor axis because we know the total mass of the system, $M_A + M_B$. There is an asymmetry in the posterior distribution of the inclination, likely due to this system being on the edge of a grazing/total eclipse (it is unclear from our data whether it is flat-bottomed or not).

Temperature constraints. The temperatures of the two WDs are constrained by an interplay of modeling the light curves and fitting the Pan-STARRS1 and Swift UVM2 photometry. This is because the ratio of eclipse depths in the light curve places stringent constraints on the surface brightness ratio and therefore the temperature ratio, whereas the SED sets the overall temperature scale. We wish to note that because of the high temperature of the objects, $T > 15{,}000$ K, most of their flux is found in the ultraviolet; thus, the Swift UVM2 photometric measurement dominates this estimate and is highly sensitive to the assumed reddening. Our solution for the temperatures is lower than that inferred from the spectroscopic modeling by about 2σ, likely due to the uncertainties in reddening. In any case, we wish to emphasize that the

spectroscopic and SED temperature estimates differ by <20%, and both estimates still give a similar physical picture of the system and its evolutionary history.

Distance constraints. The distance is primarily constrained by the fit to the SED, since the overall flux contribution of each WD to the SED photometry depends only on $\frac{R}{d}$. The light-curve fit is not directly sensitive to the distance, but it does constrain the ratio of the radii and temperature of the two WDs used in computing the synthetic photometry, as discussed above. The distance we estimate to the system, $d = 2425^{+109}_{-115}$, is consistent with that of the nearby bright star to the northwest seen in Figure 2, which has a Gaia parallax of $\bar{\omega} = 0.479 \pm 0.024$ mas; however, uncertainties in the astrometric solution are currently too large to establish an association (if associated, the objects would be separated by ∼15,000 au).

3.5. Spectroscopic Modeling

The phase-resolved spectra revealed that ZTF J2243+5242 is a double-lined spectroscopic binary that consists of two hydrogen-rich (DA) WDs (see Figure 4). Due to the limited S/N of the phase-binned spectra we acquired, our radial velocity estimates from these data are more uncertain than the light-curve modeling and rather sensitive to parameters such as the assumed surface gravity and reddening. The low S/Ns of the spectra are a consequence of the faint nature of the object, the short exposure time needed to preserve temporal resolution, and large readout duty cycle of the observations.

We fit the spectra in order to estimate the effective temperatures of the WDs in the system. We use the synthetic DA NLTE WD atmospheric models described in Tremblay et al. (2011), with stark broadening from Tremblay & Bergeron (2009). We generate a composite WD spectrum by using the ratio of the radii of the two components inferred from light-curve modeling to weight each component's flux appropriately and also fix the ratio of the temperatures of the two components based on light-curve modeling (as the relative depth of the eclipses constrains this quite well). We also fixed the surface gravities of both objects based on masses and radii inferred from light-curve modeling. We use the masses estimated from the light-curve analysis to appropriately Doppler shift the spectral components of each WD based on the phase of each spectrum.

By fitting the spectra with these model atmospheres, we estimate temperatures of $T_A = 26{,}520 \pm 130$ and $T_B = 19{,}670 \pm 100$ K. These estimates are more precise than those estimated from the SED alone, and we report them here as a point of reference to compare the estimates from our combined analysis (see Table 3), which are based on the SED alone. We take both approaches to illustrate the feasibility of estimating temperature from just the SED, as this will be far more practical for the large number of faint WDs discovered by VRO and LISA than attempting spectroscopic follow-up of these systems. An example of a fit of the spectrum of the object is illustrated in Figure 4. Note that such an estimate is mainly feasible for eclipsing systems, in which the relative luminosity and radii of the two components can be constrained.

We estimated the masses of the two components by summing all spectra with phases near quadrature where the Doppler shift of each object as viewed from Earth is at a maximum. These stacked spectra at quadrature were constructed from taking a weighted sum of spectra with mid-exposure phases falling between 0.2 and 0.3 and the other stack using spectra with mid-exposures between phases 0.7 and 0.8. We then analyzed each of the two stacks at quadrature using a boostrapping technique, where we resampled the flux at each wavelength according to the corresponding error bar, and we performed 1000 iterations of this to estimate the uncertainty in our mass estimates. We performed 1000 iterations on the coaddition at phases 0.2–0.3 and 0.7–0.8 and estimated the uncertainties by combining all of the results of this boostrapping exercise. The results of this analysis are $M_A = 0.308^{+0.074}_{-0.074}$ and $M_B = 0.274^{+0.047}_{-0.047}\,M_\odot$, which are consistent with the masses estimated using the photometric analysis. The estimated masses were sensitive to how we treated the estimated surface gravity of each object (the estimates we report fixed the quantity based on estimates from the light-curve modeling, but if we instead computed it based on the fit mass and fixed radius, our estimates shifted). Additionally, because we fit the entire flux-calibrated spectrum (from 3700 to 5000 Å) without introducing any additional normalization of the continuum, we found that the estimated masses were sensitive to factors such as assumed reddening. Because the mass estimates should depend only on the Doppler shift of the Balmer lines and not a factor such as reddening, we repeated the fit locally around each Balmer line and also conducted a global fit, where we introduced the reddening as a free parameter rather than fixing it (effectively allowing the fit to best match the full spectral model across the entire wavelength range). We found that the analysis locally around the Balmer lines agreed well with our full fit of the lines+continuum in the case where reddening was allowed to be a free parameter; however, the best-fit model estimated a reddening of $E(g - r) = 0.27 \pm 0.03\,m_{AB}$, noticeably larger than that reported by Green et al. (2019). With this value of reddening, which best fits the full spectrum, we estimate a temperature of $T_A = 28{,}400 \pm 560$ and $T_B = 20{,}700 \pm 400$ K for the hotter WD, indicating that it is possible that the temperatures may be slightly higher than those reported in Table 3 if the reddening of Green et al. (2019) is indeed an underestimate (it is also possible that the flux calibration is imperfect and that the discrepancy in reddening arises from this).

4. Discussion

4.1. Evolutionary History

Given the masses reported in Table 3, it is likely that the system consists of a pair of He WDs, though the uncertainties do allow for masses potentially consistent with either carbon–oxygen (CO) or hybrid WDs (Perets et al. 2019). If the system is indeed a pair of He WDs, one evolutionary channel from which ZTF J2243+5242 could have formed is via an episode of stable mass transfer, followed by a common envelope event. There is a tight relation between the radius of a star ascending the red giant branch and its He core mass and thus a close relationship between the mass of an He WD and the orbital period at which its progenitor star underwent a mass-transfer event, stripping it of its envelope (Rappaport et al. 1995). Rappaport et al. (1995) estimated the relation as

$$P_{\rm orb} = 1.3 \times 10^5 M_{\rm WD}^{6.25}/(1 + 4M_{\rm WD}^4)^{1.5}\ {\rm days}, \quad (3)$$

where $P_{\rm orb}$ is the orbital period at the start of the mass-transfer event that forms the He WD, and $M_{\rm WD}$ is the mass of the remnant He WD in solar masses. This suggests that the progenitor of ZTF J2243+5242 underwent a common envelope

event at an orbital period of ≈160 days, with an initial orbital period somewhat shorter due to the orbital widening that occurred during the preceding stable mass-transfer phase.

For a detached compact binary that has a measured $\dot{P}_b$, if one assumes that the system is undergoing orbital decay due to general relativity and can determine a cooling age, one can estimate the orbital period that the system exited the common envelope by extrapolating the orbital evolution back in time.

In order to estimate the orbital period at which the system might have exited the common envelope, we modeled the evolution of the primary WD with MESA using its precomputed WD model with $M = 0.35\,M_{\odot}$. Using this model, we estimate that the system is roughly 17 million yr old and exited the common envelope phase with an orbital period of 36 minutes, which is consistent with the observation from the ELM survey that most close He WD binaries emerge from the common envelope phase at orbital periods under 1 hr (Brown et al. 2016b). The actual age and initial orbital period could be slightly longer if diffusion and/or rotational mixing processes allow for more extended hydrogen burning or hydrogen shell flashes (Althaus et al. 2013). Based on the models of Istrate et al. (2016), these processes last less than 10 Myr in a WD of this mass, so the system is very likely younger than 30 Myr and was born at an orbital period of less than 1 hr.

A caveat to this calculation is that tidal heating may contribute significantly to the luminosity of the WDs in ZTF J2243+5242 and thus may impact our age estimates. From Burdge et al. (2019a), the upper limit to the surface temperature produced by tidal heating is $T_{\rm tide} = (\pi\kappa M\dot{P}/2\sigma_B P^3)^{1/4} \approx 30{,}000$ K for each of the WDs in ZTF J2243+5242. In a more realistic estimate for tidal heating, which accounts for the expected near spin–orbit synchronism, the tidal heating rate is reduced by roughly an order of magnitude, so the tidal temperature will be closer to $T_{\rm tide} \sim 18{,}000$ K. Hence, it is quite possible that the luminosity of the secondary is dominated by tidal heat. While tidal heating may contribute to the luminosity of the primary, its significantly higher temperature (despite a similar mass and radius) suggests that its luminosity is dominated by normal WD cooling, validating the young age estimate above. Hence, these rapidly merging systems may spend only a tiny fraction of their lives as DWDs.

4.2. Future Evolution

Object ZTF J2243+5242 is undergoing rapid orbital decay. The system is currently clearly detached, with $\frac{R}{R_L} \approx \frac{2}{3}$ for both components; however, the two components will start interacting in approximately 320,000 yr, likely evolving into a direct impact accretor and bright source of X-rays like HM Cnc and V407 Vul. Based on the mass ratio of the system, mass transfer will likely be unstable (Marsh et al. 2004), and the system will merge in <400,000 yr. After merger, the system is likely to form either an isolated hot subdwarf star or an R Coronae Borealis star. In any case, the remnant of this merger will eventually cool to form an ∼0.5–0.7 $M_{\odot}$ CO WD on the WD cooling track, which may be rapidly rotating. Merging pairs of He WDs like ZTF J2243+5242 demonstrate that some "normal-mass" CO WDs with $M \sim 0.6\,M_{\odot}$ likely form from merger events.

4.3. Implications for LISA and the VRO

As demonstrated in this work, using just photometric measurements, we were able to estimate component parameters for ZTF J2243+5242, including masses, temperatures, and radii, as well as orbital parameters, such as inclination, period, orbital period decay rate, time of superior conjunction, and semimajor axis. This has major implications for the eras of the VRO (Ivezić et al. 2019) and LISA (Amaro-Seoane et al. 2017), which we discuss here.

LISA and the VRO are both expected to significantly increase the number of known short-period DWDs. The VRO is an upcoming optical southern-sky synoptic survey using the Simonyi Survey Telescope, which has an effective aperture of 6.5 m, and the instrument has a field of view of 9.6 deg^2, about a quarter of ZTF's (Ivezić et al. 2019). The survey is expected to reach a 5σ depth of approximately 24.5 in r in a 30 s exposure, about 4 mag fainter than ZTF.

The VRO, with its smaller field of view, will acquire about a quarter of the number of samples of the ZTF in an equivalent survey time and thus will not perform as well in recovering periodic objects at the same S/N. By the time the survey does reach a comparable number of samples to the ZTF after 2.5 yr, which should take the VRO about a decade or so, the frequency evolution of these objects will make it impossible to recover them without acceleration searches (Katz et al. 2020). The VRO could partially compensate for this by adopting two 15 s exposures rather than a single 30 s one, as this not only doubles the number of epochs for such sources but actually provides a crucial ingredient: high time resolution. Such exposures would be consecutive, effectively measuring both the flux and its derivative at a given time (which, for points in eclipse, is very valuable). Eclipsing DWDs such as ZTF J2243+5242 and ZTF J1539+5027 can significantly change their brightness in <15 s during the ingress and egress of their primary eclipse, so such a measurement would be highly sensitive to this kind of rapid photometric variability, greatly enhancing the facility's discovery capabilities in ultrafast-timescale optical variability. The other fundamental challenge is that the VRO will divide its exposures into many filters, complicating period finding (an important element in preparing for this survey will be to adapt a wide range of algorithms to cope with this technical challenge; VanderPlas 2018).

The VRO should contribute significantly to the discovery of low- and moderate-amplitude sources like ZTF J2243+5242 at <23.0 in r, where improved photometric precision can partially compensate for the lack of temporal resolution compared to more densely sampled surveys, such as the ZTF. These binaries will be so faint that obtaining phase-resolved spectroscopy for more than a handful will be impossible without substantial time on an extremely large telescope (ELT). Our analysis of ZTF J2243+5242 gives hope that it will be feasible to characterize the photometrically variable systems among these without depending on spectroscopic follow-up. As discussed above, we were able to constrain many parameters in this system using just photometric measurements; this means that the large number of faint eclipsing binaries discoverable by the VRO (and eventually LISA) could be characterized simply by obtaining a single high-S/N light curve on a high-speed photometer and combining modeling of this light curve with a measurement of $\dot{P}_b$ using the longer-baseline VRO data, or in some cases, such modeling could be possible using just the VRO light curves alone. Such purely photometric analyses

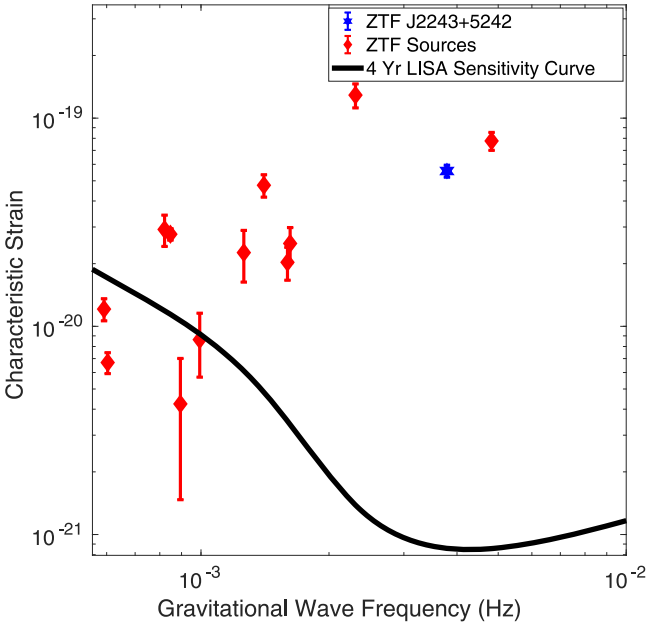

Figure 7. Current ZTF sample of ultracompact binary sources reported in Burdge et al. (2020; red diamonds). The blue star indicates ZTF J2243+5242, the second shortest period system shown here. Because the power spectral density of LISA's sensitivity curve is expected to increase substantially at a frequency corresponding to around 15 minutes, sources below this period, like ZTF J0538+1953, ZTF J2243+5242, and ZTF J1539+5027, should all be detected by LISA with high S/N, enabling precise parameter estimation using gravitational waves. It is worth noting that these high-S/N sources are all eclipsing binaries, making them particularly valuable astrophysical laboratories.

open up the possibility of characterizing a large population of such systems, and identifying properties such as masses/core compositions, which have implications for both the binary evolutionary processes which form these systems, and also the outcomes of the interactions/mergers.

In the era of LISA, short orbital period systems like ZTF J2243+5242 and ZTF J1539+5027 will be particularly valuable astrophysical laboratories. Because these systems fall near the peak of LISA's sensitivity (see Figure 7), they are detectable at large distances (ZTF J2243+5242 reaches an S/N of 7 in LISA at ≈20 kpc and ZTF J1539+5027 at ≈30 kpc). LISA, which will be unhindered by Galactic extinction, should easily detect most of these kinds of objects in the Milky Way.

One way to prepare for LISA is by developing ground- and space-based instrumentation optimized to best characterize the optically detectable portion of its source population in an efficient manner. We hope that in this work, Burdge et al. (2019a, 2019b, 2020), and Coughlin et al. (2020), we have demonstrated that high-speed photometers, which can obtain densely sampled high-S/N light curves with high temporal resolution, will be one of the most powerful tools for such characterization. Such instruments on 10 and 30 m class telescopes could be used to characterize binaries like ZTF J2243+5242 and ZTF J1539+5027 to 10–30 kpc, distances well matched to LISA's sensitivity threshold.

5. Conclusion

Here we described the discovery and characterization of ZTF J2243+5242, the second eclipsing binary known with an orbital period under 10 minutes. The system is a DWD with an orbital period of just 8.8 minutes and will be a strong LISA gravitational-wave source. We performed a comprehensive analysis of the system using just photometric measurements, demonstrating the considerable value of photometry as a tool not just for discovering such extreme systems but that can also be used to precisely characterize these objects at great distances and faint apparent magnitudes. We were able to determine that ZTF J2243+5242 likely consists of two He WDs that will merge in approximately 400,000 yr, with component masses of $M_A = 0.323^{+0.065}_{-0.047}$ and $M_B = 0.335^{+0.052}_{-0.054}\ M_\odot$.

The ZTF has already significantly altered the landscape of the extremely short orbital period binary systems known in the Galaxy and will continue to do so as it acquires more epochs during ZTF Phase II and receives improvements to its archival photometry. The current discoveries mark the beginning of a golden era for discovering these objects, a sample that will profoundly alter our understanding of compact binary evolution as we continue to discover more of them and understand both the processes that lead to their creation and their eventual fates upon merger.

K.B.B. thanks the National Aeronautics and Space Administration and the Heising-Simons Foundation for supporting his research. K.B.B. also wishes to thank Andrew Tisdale for his generous contribution to this research effort. M.W.C. acknowledges support from the National Science Foundation with grant No. PHY-2010970. J.F. acknowledges support from an Innovator Grant from the Rose Hills Foundation and the Sloan Foundation through grant FG-2018-10515. T.R.M. was supported by the UK's Science and Technology Facilities Council through grant ST/T000406/1. We wish to thank the referee of this work for their excellent suggestions, which have considerably enhanced the quality of the work.

Based on observations obtained with the Samuel Oschin Telescope 48 inch and the 60 inch telescope at the Palomar Observatory as part of the Zwicky Transient Facility project. The ZTF is supported by the National Science Foundation under grant No. AST-1440341 and a collaboration including Caltech, IPAC, the Weizmann Institute for Science, the Oskar Klein Center at Stockholm University, the University of Maryland, the University of Washington, Deutsches Elektronen-Synchrotron and Humboldt University, Los Alamos National Laboratories, the TANGO Consortium of Taiwan, the University of Wisconsin at Milwaukee, and Lawrence Berkeley National Laboratories. Operations are conducted by the COO, IPAC, and UW.

Some of the data presented herein were obtained at the W. M. Keck Observatory, which is operated as a scientific partnership among the California Institute of Technology, the University of California, and the National Aeronautics and Space Administration. The Observatory was made possible by the generous financial support of the W. M. Keck Foundation. The authors wish to recognize and acknowledge the very significant cultural role and reverence that the summit of Maunakea has always had within the indigenous Hawaiian community. We are most fortunate to have the opportunity to conduct observations from this mountain.

The ZTF forced-photometry service was funded under Heising-Simons Foundation grant 12540303 (PI: Graham).

Facilities: PO:1.2 m (ZTF), Hale (CHIMERA), Keck:I (LRIS), Swift (XRT and UVOT).

Software: Aplpy (Robitaille & Bressert 2012), Astropy (Astropy Collaboration et al. 2013), CUVARBASE (https://

github.com/johnh2o2/cuvarbase), LCURVE (Copperwheat et al. 2010), Lpipe (Perley 2019), Multinest (Feroz et al. 2009), Numpy (van der Walt et al. 2011).

ORCID iDs

Kevin B. Burdge https://orcid.org/0000-0002-7226-836X
Michael W. Coughlin https://orcid.org/0000-0002-8262-2924
Jim Fuller https://orcid.org/0000-0002-4544-0750
David L. Kaplan https://orcid.org/0000-0001-6295-2881
S. R. Kulkarni https://orcid.org/0000-0001-5390-8563
Thomas R. Marsh https://orcid.org/0000-0002-2498-7589
Eric C. Bellm https://orcid.org/0000-0001-8018-5348
Richard G. Dekany https://orcid.org/0000-0002-5884-7867
Dmitry A. Duev https://orcid.org/0000-0001-5060-8733
Matthew J. Graham https://orcid.org/0000-0002-3168-0139
Ashish A. Mahabal https://orcid.org/0000-0003-2242-0244
Frank J. Masci https://orcid.org/0000-0002-8532-9395
Russ R. Laher https://orcid.org/0000-0003-2451-5482
Reed Riddle https://orcid.org/0000-0002-0387-370X
Maayane T. Soumagnac https://orcid.org/0000-0001-6753-1488
Thomas A. Prince https://orcid.org/0000-0002-8850-3627

References

Althaus, L. G., Miller Bertolami, M. M., & Córsico, A. H. 2013, A&A, 557, A19
Amaro-Seoane, P., Audley, H., Babak, S., et al. 2017, arXiv:1702.00786
Astropy Collaboration, Robitaille, T. P., Tollerud, E. J., et al. 2013, A&A, 558, A33
Bellm, E. C., Kulkarni, S. R., Graham, M. J., et al. 2019, PASP, 131, 018002
Brown, W. R., Gianninas, A., Kilic, M., Kenyon, S. J., & Allende Prieto, C. 2016a, ApJ, 818, 155
Brown, W. R., Kilic, M., Allende Prieto, C., Gianninas, A., & Kenyon, S. J. 2013, ApJ, 769, 66
Brown, W. R., Kilic, M., Allende Prieto, C., & Kenyon, S. J. 2010, ApJ, 723, 1072
Brown, W. R., Kilic, M., Allende Prieto, C., & Kenyon, S. J. 2012, ApJ, 744, 142
Brown, W. R., Kilic, M., Kenyon, S. J., & Gianninas, A. 2016b, ApJ, 824, 46
Brown, W. R., Kilic, M., Kosakowski, A., et al. 2020, ApJ, 889, 49
Burdge, K. B., Coughlin, M. W., Fuller, J., et al. 2019a, Natur, 571, 528
Burdge, K. B., Fuller, J., Phinney, E. S., et al. 2019b, ApJL, 886, L12
Burdge, K. B., Prince, T. A., Fuller, J., et al. 2020, ApJ, 905, 32
Chambers, K. C., Magnier, E. A., Metcalfe, N., et al. 2016, arXiv:1612.05560
Claret, A. 2000, A&A, 363, 1081
Claret, A., Cukanovaite, E., Burdge, K., et al. 2020a, A&A, 634, A93
Claret, A., Cukanovaite, E., Burdge, K., et al. 2020b, arXiv:2007.15715
Copperwheat, C. M., Marsh, T. R., Dhillon, V. S., et al. 2010, MNRAS, 402, 1824
Coughlin, M. W., Burdge, K., Phinney, E. S., et al. 2020, MNRAS, 494, L91
Dekany, R., Smith, R. M., Riddle, R., et al. 2020, PASP, 132, 038001
Feroz, F., Hobson, M. P., & Bridges, M. 2009, MNRAS, 398, 1601
Gehrels, N., Chincarini, G., Giommi, P., et al. 2004, ApJ, 611, 1005
Gianninas, A., Kilic, M., Brown, W. R., Canton, P., & Kenyon, S. J. 2015, ApJ, 812, 167
Graham, M. J., Drake, A. J., Djorgovski, S. G., Mahabal, A. A., & Donalek, C. 2013, MNRAS, 434, 2629
Graham, M. J., Kulkarni, S. R., Bellm, E. C., et al. 2019, PASP, 131, 078001
Green, G. M., Schlafly, E., Zucker, C., Speagle, J. S., & Finkbeiner, D. 2019, ApJ, 887, 93
Harding, L. K., Hallinan, G., Milburn, J., et al. 2016, MNRAS, 457, 3036
Istrate, A. G., Marchant, P., Tauris, T. M., et al. 2016, A&A, 595, A35
Ivezić, Ž, Kahn, S. M., Tyson, J. A., et al. 2019, ApJ, 873, 111
Katz, M. L., Cooper, O. R., Coughlin, M. W., et al. 2020, arXiv:2006.06866
Kilic, M., Brown, W. R., Allende Prieto, C., et al. 2011, ApJ, 727, 3
Kilic, M., Brown, W. R., Allende Prieto, C., et al. 2012, ApJ, 751, 141
Littenberg, T. B., & Cornish, N. J. 2019, ApJL, 881, L43
Marsh, T. R., Nelemans, G., & Steeghs, D. 2004, MNRAS, 350, 113
Masci, F. J., Laher, R. R., Rusholme, B., et al. 2019, PASP, 131, 018003
Morris, S. L. 1985, ApJ, 295, 143
Napiwotzki, R., Christlieb, N., Drechsel, H., et al. 2003, Msngr, 112, 25
Napiwotzki, R., Karl, C. A., Lisker, T., et al. 2020, A&A, 638, A131
Oke, J. B., Cohen, J. G., Carr, M., et al. 1995, PASP, 107, 375
Perets, H. B., Zenati, Y., Toonen, S., & Bobrick, A. 2019, arXiv:1910.07532
Perley, D. A. 2019, PASP, 131, 084503
Piro, A. L. 2019, ApJL, 885, L2
Ramsay, G., Hakala, P., & Cropper, M. 2002, MNRAS, 332, L7
Rappaport, S., Podsiadlowski, P., Joss, P. C., Di Stefano, R., & Han, Z. 1995, MNRAS, 273, 731
Robitaille, T., & Bressert, E. 2012, APLpy: Astronomical Plotting Library in Python, Astrophysics Source Code Library, ascl:1208.017 https://aplpy.github.io/
Taylor, J. H., & Weisberg, J. M. 1989, ApJ, 345, 434
Tremblay, P. E., & Bergeron, P. 2009, ApJ, 696, 1755
Tremblay, P. E., Bergeron, P., & Gianninas, A. 2011, ApJ, 730, 128
van der Walt, S., Colbert, S. C., & Varoquaux, G. 2011, CSE, 13, 22
VanderPlas, J. T. 2018, ApJS, 236, 16
Yao, Y., Miller, A. A., Kulkarni, S. R., et al. 2019, ApJ, 886, 152